

PB-NBV: Efficient Projection-Based Next-Best-View Planning Framework for Reconstruction of Unknown Objects

Zhizhou Jia, Yuetao Li, Qun Hao, and Shaohui Zhang

Abstract—Completely capturing the three-dimensional (3D) data of an object is essential in industrial and robotic applications. The task of next-best-view (NBV) planning is to calculate the next optimal viewpoint based on the current data, gradually achieving a complete 3D reconstruction of the object. However, many existing NBV planning algorithms incur heavy computational costs due to the extensive use of ray-casting. To address this, we propose a projection-based NBV planning framework. Specifically, this framework refits different types of voxel clusters into ellipsoids based on the voxel structure. Then, the next optimal viewpoint is selected from the candidate views using a projection-based viewpoint quality evaluation function in conjunction with a global partitioning strategy. This process replaces extensive ray-casting, significantly improving the computational efficiency. Comparison experiments in the simulation environment show that our framework achieves the highest point cloud coverage with low computational time compared to other frameworks. The real-world experiments also confirm the efficiency and feasibility of the framework. Our method will be made open source to benefit the community¹.

I. INTRODUCTION

Acquiring the complete and high-quality 3D geometric structure of an object is crucial for reverse engineering and quality inspection in industrial applications, as well as for autonomous exploration and interaction in robotics. In practical scanning, achieving a complete scan can be challenging due to occlusions or limitations in the acquisition device’s field of view (FOV). In response, Connolly [1] first introduced a strategy that leverages the observed data to identify the next optimal scanning viewpoint for achieving a comprehensive object scan, known as the NBV planning problem. As research on the NBV planning problem advanced, it was gradually modeled into three core components: object representation, candidate viewpoint proposal, and optimal viewpoint selection.

In many existing algorithms, once the object is represented by a voxel structure, the ray-casting algorithm is typically used to assess the visibility of each candidate viewpoint to the object [2]–[5]. This algorithm involves emitting multiple rays from each candidate viewpoint and examining the occlusion of each ray with the target structure. However, this process involves numerous queries, and as the object’s volume and precision requirements increase, the use of the ray-casting algorithm imposes a significant computational burden [6]–[8], limiting the deployment of the NBV planning algorithm on lightweight edge computing robot platforms.

All authors are with the School of Optics and Photonics, Beijing Institute of Technology, Beijing 100081, China. (Corresponding author: Shaohui Zhang.) {jiazhizhou, liyuetaochn, qhao, zhangshaohui}@bit.edu.cn

¹To be released at: https://github.com/dspangpang/pb_nbv

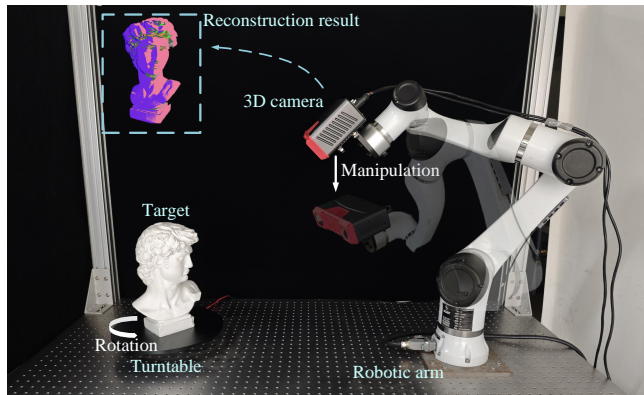


Fig. 1. Overview of the NBV planning experiment platform. An object to be measured is placed on a turntable, and a 3D camera is equipped at the end of the robotic arm for data acquisition. Our NBV planning framework accomplishes a complete reconstruction of the object by controlling the robotic arm and the turntable.

To address this issue, we propose a novel projection-based NBV planning framework. The framework is based on voxel structures, where the voxels are further fitted into ellipsoids. When selecting the next optimal viewpoint, an ellipsoid-based independent projection strategy for evaluating observation quality replaces ray-casting, significantly reducing the computational burden caused by an increase in object volume or higher precision requirements for the representation structure. The framework also introduces a global partitioning strategy to ensure the success of point cloud registration between frames and reduce backtracking caused by greedy viewpoint selection.

To evaluate the performance of our framework, we set up a simulation environment for ablation studies and comparisons with existing mainstream NBV frameworks. Additionally, the real-world experiments also confirm the efficiency and feasibility of the framework. The experiments were conducted in a real-world setup similar to SEE [8], as shown in Fig. 1.

In summary, the main contributions of this paper are the following three:

- 1) We propose an ellipsoid-fitting-based representation structure for unknown objects, enabling dimensionality reduction of voxel structures while retaining essential information.
- 2) We propose an ellipsoid-based projection algorithm to replace the ray-casting in selecting the next optimal viewpoint, significantly reducing the computational burden.
- 3) We introduce a global partitioning strategy to ensure point cloud registration success and reduce the impact of

backtracking from greedy selection on efficiency.

II. RELATED WORKS

Currently, the NBV planning problem is typically modeled into three core components: object representation, candidate viewpoint proposal, and optimal viewpoint selection. Research has proposed various solutions and strategies by optimizing and innovating these components.

A. *object representation*

Object representation is a fundamental aspect of the NBV planning problem; different representation methods directly affect the accuracy and efficiency of the overall NBV planning framework. The object representation, ranging from simple to complex, typically include point clouds [8]–[10], voxels [1]–[7, 11]–[15], and surface [16]–[18] structures. With the advancement of computer graphics, emerging structures such as Implicit Neural Representations (INR) [19]–[21] are also being utilized to describe NBV planning problems. Voxel structures are commonly used for object representation due to their simplicity, intuitiveness, and controllable precision.

B. *candidate viewpoint proposal*

Finding an optimal 6-DOF viewpoint directly through optimization in space is very challenging, so researchers usually sample a number of candidate viewpoints and then choose the best one. Currently, common candidate viewpoint sampling strategies can generally be categorized into four types: random sampling [2, 3], predefined set [1, 6, 7], path-based sampling [5, 13]–[15], and scene-information-based sampling [4, 8]. The candidate viewpoint sampling strategy should be appropriately adjusted according to the current holistic data acquisition system. An appropriate strategy will enhance the convergence efficiency of the NBV planning framework.

C. *Optimal viewpoint selection*

It's hard to tell which areas have more potential information just from the object's structure (which only includes position data). To measure this information, researchers usually classify each structural unit by the sensor's observation pose; different units indicate varying levels of potential information in their areas. The strategy for selecting candidate viewpoints aims to maximize this potential information.

Optimal viewpoint selection strategies for different NBV problems and scenarios can be divided into those focusing on completeness and those focusing on efficiency.

1) *Completeness-focused strategies*: Focusing on voxel structures, the optimal viewpoint selection strategies that emphasize completeness are primarily divided into position-based classification [4, 5, 12, 13, 15], occupancy probability-based classification [3], and a combination of both [2].

Position-based classification focuses on edge information and classifies frontier units representing edge locations from all representation units. The optimal viewpoint should capture the maximum number of Frontier units. The occupancy

probability method determines the probability of each representation unit being a solid object, using information entropy theory to judge which viewpoint will bring the greatest information gain. The combined strategy first classifies the representation units, then assigns different occupancy probabilities to different units, and finally selects the optimal viewpoint through information gain. Also, some strategies incorporate practical environmental constraints and use utility functions to adjust greedy indicators, preventing robots from being unable to reach certain viewpoints [11].

2) *Efficiency-focused strategies*: In the process of selecting the optimal viewpoint, the potential information of each candidate viewpoint must be calculated iteratively. The commonly used ray-casting algorithm judges the visibility of units by emitting multiple rays, but it poses a significant computational burden when dealing with complex structures. Efficiency strategies aim to address these issues.

The first category of strategies focuses on simplifying the representation structure by directly analyzing potential information at the point cloud level [8]–[10], thereby reducing the time spent on structure construction and visibility queries.

The second category of strategies enhances the efficiency of ray-casting. Both [11] and [5] propose strategies to improve the efficiency of ray-casting itself. [22] uses GPU to accelerate ray-casting. Some deep learning strategies can avoid using ray-tracing algorithms and provide the best viewpoint at a fast speed. [6] and [9] use the network to predict the information gain for selecting the next perspective. [7] can infer all subsequent observation viewpoints by inputting only one frame of observation. However, generalizing such algorithms to other unknown objects that differ from their training set is challenging [8].

Inspired by previous research and the 3D Gaussian Splatting method [23], we propose an NBV planning framework based on voxel structures. The framework consolidates classified frontier and occupied voxels into an ellipsoid and evaluates the potential observation quality of viewpoints through projection. It completely replaces ray-casting in the process of candidate viewpoint evaluation, significantly improving computational efficiency. The next section will elaborate on the specifics of this framework in detail.

III. METHODOLOGY

A. *Framework Overview*

The workflow of our projection-based NBV planning framework is shown in Fig 2. The robot arm first moves to a preset initial observation pose and then starts the iterative process of NBV planning.

B. *Proposal of Candidate Viewpoints*

As shown in Fig. 1 of the experimental setup, we assume that the bounding box radius of the object to be reconstructed will not exceed the distance from the robotic arm base to the turntable. Considering the depth of field limitations of the 3D camera, we propose a strategy to dynamically adjust the candidate view sampling area to ensure complete

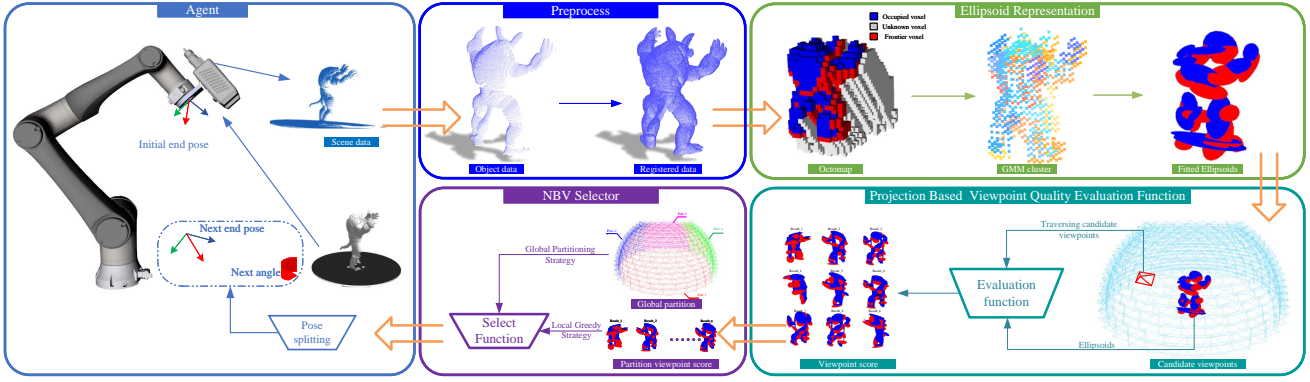


Fig. 2. Overview of NBV planning framework. The orange arrows describe the running steps of the NBV iteration process. After capturing the point cloud, the framework performs preprocessing and pose registration. The registered point cloud is then input into the ellipsoid representation module, where it is converted into a voxel structure and fitted into an ellipsoid. The projection evaluation function is used to assess all candidate viewpoints, and a global partitioning strategy selects the optimal viewpoint for the next frame. Finally, the robotic arm moves to the selected viewpoint and begins the next iteration.

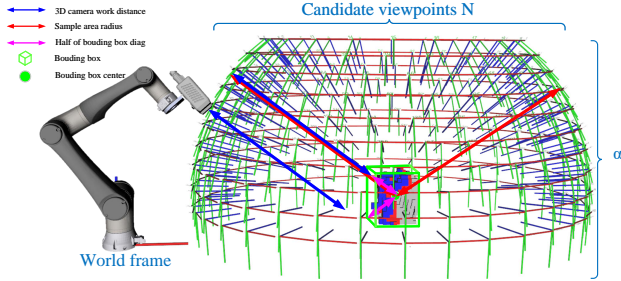


Fig. 3. The components of the radius of the candidate viewpoint sampling region and the results of candidate viewpoint sampling within this region.

reconstruction of the object within the optimal shooting distance of the 3D camera.

Considering the reachability of the robot arm, we set the sampling area of the candidate viewpoint to the partial hemisphere area above the turntable. The algorithm uses the base coordinates of the robot as the world coordinate system, as shown in Fig. 3. The radius of this hemisphere R is the sum of the 3D camera's working distance d_c and half the diagonal length of the unknown object's bounding box d_b . As the bounding box of the object changes during reconstruction, the size of the hemisphere is dynamically adjusted to accommodate the depth of field limitations of the 3D camera.

We selected α equidistant parallels from the candidate area and distributed N candidate viewpoints proportionally along each parallel based on their lengths. All viewpoints are directed toward the center of the bounding box.

C. Voxel Structure construction

After the 3D camera captures a point cloud frame, the framework first performs preprocessing on the data. The pre-processed point cloud is then registered into the point cloud set P_f and subjected to voxel construction. We categorize voxels within the unknown object's bounding box into five

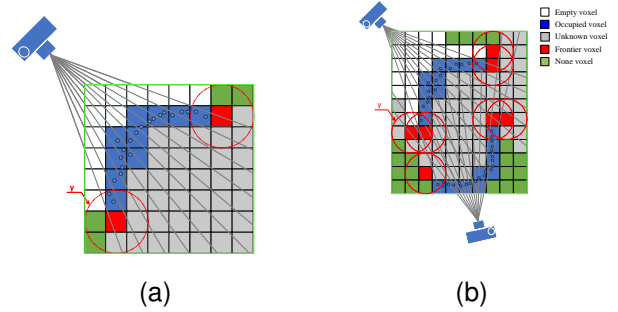


Fig. 4. Use a 2D grid to describe the voxel classification. (a) Classification results of a single frame input. (b) Classification results of multiple frames input. The green box represents the object's bounding box.

types: Empty V_e , Occupied V_o , Unknown V_u , Frontier V_f , and None V_n , as shown in Fig. 4.

Each time the bounding box is updated, the newly added voxels are initially set to V_n , indicating voxels have not been scanned by the device. V_o represents the surface structure of the unknown object, which is the voxel occupied by P_f . V_e represents the free area in the bounding box, which is the set of voxels not occupied by P_f after being scanned by the device. Once V_o and V_e are determined, they remain unchanged. V_u represents the area where the surface structure of the unknown object may exist. These areas are not captured by the acquisition device because they are blocked by V_o . As shown in Fig. 4(a), With each new addition of occupied voxels V_o , V_u and V_e will be generated accordingly.

We employ [24] to sample rays at equal angles within the FOV of the current viewpoint. In the voxels intersected by the ray, we distinguish between empty voxels V_e and unknown voxels V_u based on whether the current ray passes through V_o . The update of V_f is carried out after the updates of V_u and V_o . Any $v_i \in V_u$ is identified as a Frontier voxel if both empty and occupied voxels are present in its spatial

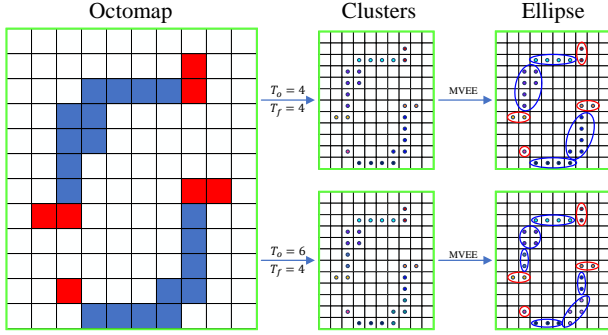


Fig. 5. Results of different GMM clustering numbers. T_o represents the number of clusters of occupied voxels, and T_f represents the number of clusters of frontier voxels.

neighborhood.

$$V_f = \{v_u^i \mid \exists v_e \in \mathcal{N}(u^i) \ \& \ v_o \in \mathcal{N}(u^i)\} \quad (1)$$

where $v_u^i \in V_u$ and $\mathcal{N}(u^i)$ represents the spatial neighborhood of v_u^i .

The bounding box \mathbf{B} is initialized to the bounding box of V_o in the first frame. Then, \mathbf{B} is expanded along the direction of the current viewpoint, doubling its diagonal length. In subsequent updates, a sphere s_i with a radius of γ is generated around each voxel $v_i \in V_f$, and the size of \mathbf{B} is expanded to cover V_o , V_u and s_i . The result is shown in Fig. 4(b).

D. Ellipsoid Representation

In 3D games, an entity’s collision structure can be represented by an ellipsoid [25], and more complex structures can be achieved by using multiple ellipsoids for different parts of an entity. Inspired by this, we also use multiple ellipsoids to describe an object structure. Since the object is unknown and its structural characteristics are unclear, it is necessary to roughly divide the object into t clusters and fit each cluster into an ellipsoid to represent the object structure. Fig. 5 illustrates this process using a two-dimensional diagram.

Inspired by 3D Gaussian Splatting [23], we know that the equiprobability density surface of a 3D Gaussian distribution is an ellipsoid. Suppose a set of points in space follows a 3D Gaussian distribution. In that case, its covariance matrix can indicate the dispersion of these points along each axis, making it easy to fit these points into an ellipsoid. Hence, we will employ a Gaussian Mixture Model (GMM) for voxel clustering.

Occupied voxels and frontier voxels will directly affect the viewpoint quality evaluation results. Therefore, after each update of V_o and V_f , we will initialize T 3D Gaussian distributions for each type of voxel (V_o and V_f). We utilize the expectation-maximization (EM) algorithm to train a Gaussian distribution, which allows us to obtain the clustering results C_o and C_f after categorizing these two types of voxels.

The selection of the number of Gaussian distributions T will directly affect the number of fitted ellipsoids in

the subsequent algorithm. Too few ellipsoids will make it difficult to accurately reflect the local structure of the object, while too many can impact the efficiency. To allow the algorithm to select the number of Gaussian distributions adaptively, we use the Bayesian Information Criterion (BIC) [26] to evaluate the model parameters.

$$\text{BIC} = k \ln(n) - 2 \ln*(L) \quad (2)$$

k is the number of model parameters, n is the number of samples, and L is the likelihood function.

The core concept of BIC is to find the best trade-off between the number of model parameters and the likelihood function value. To balance efficiency and accuracy, we set the value range of T to $[0, T_{max}]$, and T_{max} is the manually set maximum ellipsoid number to be fitted. Among the two voxels V_o, V_f , select T_o, T_f with the smallest corresponding BIC value as the number of Gaussian distributions T_* in the current iteration, that is:

$$T_* = \arg \min_{T_{max}} \text{BIC}(\text{GMM}(V, T)) \quad (3)$$

After obtaining C_o and C_f , we use the method [27] in the CGAL library to calculate the minimum-volume enclosing ellipsoids (MVVE) model. Then, we can obtain E_o and E_f , representing the fitting results of the Occupied voxels and Frontier voxels. At this point, we can transform the representation of the object from a voxel structure to an ellipsoid structure. Each ellipsoid is described by its equation.

E. Projection-based Viewpoint Quality Evaluation Function

The goal of the viewpoint quality evaluation function proposed in this paper is to enable the viewpoint to observe the most frontier information. In this process, we must consider the occlusion problem between structures when observing the object. Although ray-casting can accurately give the occlusion relationship of each voxel, the extensive use of ray-casting will take up a lot of computing resources. To address this, we use a new strategy that calculates the observable weight by using the order of the center positions of each ellipsoid under the current viewpoint. Then, the final viewpoint evaluation result is obtained by accumulating the results of individually weighted projections of each ellipsoid. The details of evaluating a single viewpoint can be divided into three parts: ellipsoid observation weight calculation, ellipsoid weighted projection calculation, and viewpoint quality result calculation.

1) *Ellipsoid observation weight calculation:* As shown in Fig. 6(a), using E_o and E_f , we can determine the position C_w of each ellipsoid center in the world coordinate system. With the camera’s pose H in the world coordinate system, we can calculate the position C of these ellipsoid centers in the camera coordinate system.

As shown in Fig. 6(b), we sort all ellipsoid centers C in ascending order according to their z-coordinates. Each ellipsoid is assigned a unique depth rank r . After obtaining the ranks, we calculate the observable weight W for each ellipsoid as follows:

$$W = 0.5^r \quad (4)$$

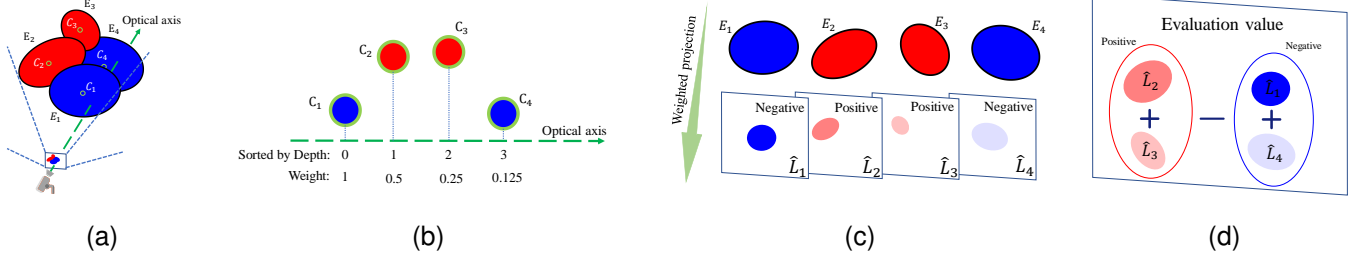


Fig. 6. Quality evaluation for a single viewpoint. (a) Transform each ellipsoid’s center to the current viewpoint’s coordinate system. (b) Sort ellipsoids by depth and assign observability weights. (c) Project each ellipsoid based on its observability weight. (d) Combine the occupied and frontier ellipsoids to obtain the viewpoint quality evaluation.

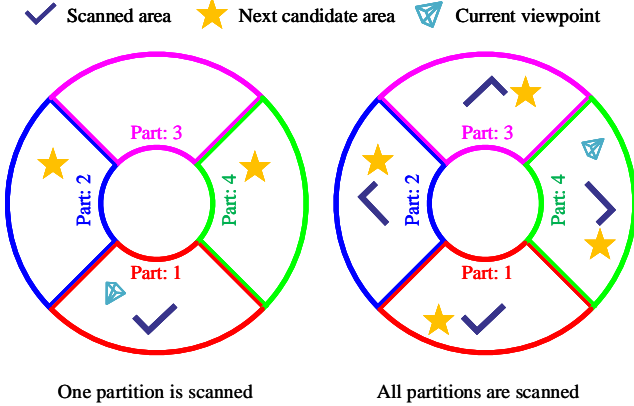


Fig. 7. This figure illustrates the process of selecting the next best view based on the scanning status of different regions.

2) *Ellipsoid weighted projection calculation:* Any ellipsoid E in space can be described by a 4th-order square matrix Q , that is:

$$X^T Q X = 0 \quad (5)$$

Where $X = [x \ y \ z \ 1]^T$. For any given ellipsoid, the ellipse it projects onto under the action of the camera projection matrix P can be represented by the matrix description Φ .

$$\Phi^* = P Q^* P^T \quad (6)$$

Where Q^* is the dual matrix of Q , Φ^* is the dual matrix of Φ . If any matrix M is a reversible matrix, its dual matrix is $M^* = M^{-1}$. The camera matrix P can be calculated by the internal parameter K of the current 3D camera, and the camera’s pose H in the world coordinate system [28].

As shown in Fig. 6(c), we project each ellipsoid individually onto the 3D camera’s imaging plane, according to the eq. 6. Then, we calculate the sum of pixel values L within each elliptical region in the image and multiply it by the observability weight w to obtain the observability of the ellipsoid, denoted as \hat{L} .

$$\hat{L} = L w \quad (7)$$

3) *Viewpoint quality evaluation function:* To maximize the observation of frontier information from the viewpoint,

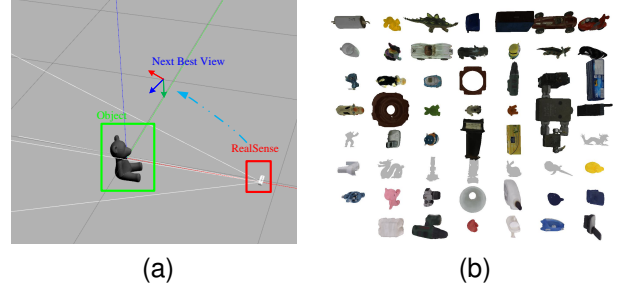


Fig. 8. Simulation environments for the comparative experiments. (a) Gazebo simulation environment. (b) Objects to be tested, 55 in total.

we need to prioritize the projection of larger frontier ellipsoids over occupied ones. For this purpose, we designed a simple evaluation function to achieve this goal:

$$F = \sum_{E_f} \hat{L} - \sum_{E_o} \hat{L} \quad (8)$$

As shown in Fig. 6(d), the projection of the frontier ellipsoid is the positive part of the observation quality assessment. In contrast, the projection of the occupied ellipsoid is the negative part. Therefore, the sum of the weighted projections of all E_f frontier ellipsoids minus the sum of the weighted projections of all E_o occupied ellipsoids can represent the quality F of the viewpoint.

F. Global partitioning strategy

Our framework needs to use the ICP [29] to correct the pose of the point cloud. Selecting the viewpoint with the highest observation quality F greedily as the best viewpoint can lead to discontinuous scanning and failure in point cloud registration. Moreover, an overly greedy selection strategy may lead to backtracking, resulting in a reduction in the efficiency of our framework.

To address this, inspired by the concept of region clustering [20], we introduce a global partitioning strategy. This strategy encompasses not only the partitioning of candidate regions but also the assurance that the viewpoint can be selected among consecutive partitions, which plays a significant role in ensuring the success rate of point cloud registration. Consecutive partitions are crucial for enhancing the success rate of point cloud registration.

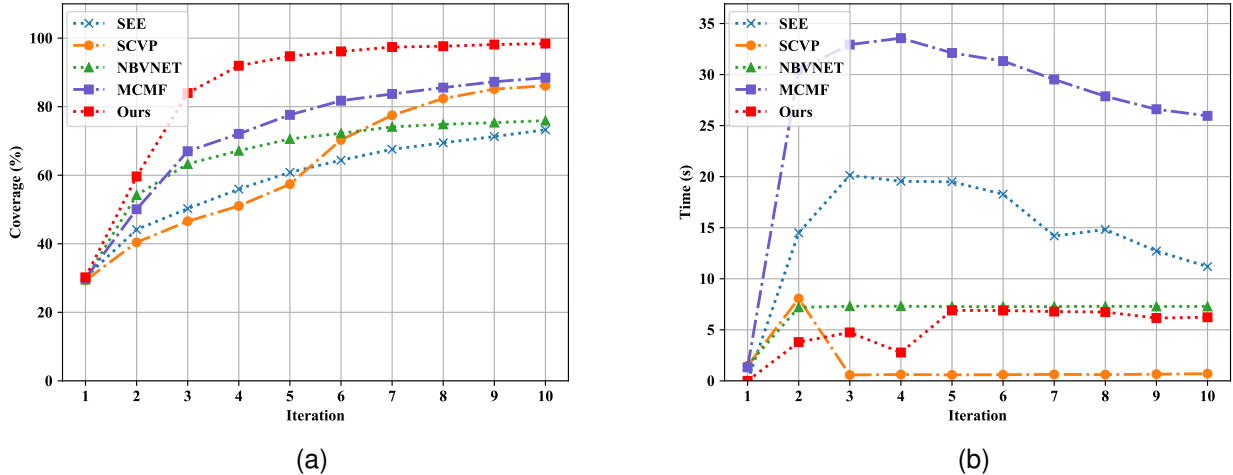


Fig. 9. The simulation results of each iteration in the comparison experiment for 55 objects. (a) Average coverage. (b) Average compute time.

We divide the candidate view sampling area into β regions according to longitude. The selection of β depends on the current registration strategy. After all regions have been scanned, the next best view can be selected from all partitions with the largest observation quality F . Otherwise, the next best view can only be selected in the unscanned neighborhood of the scanned partition, as shown in Fig. 7.

IV. EXPERIMENTS

A. Simulation experiment

To evaluate the performance of our framework, we constructed a simulation environment using the Gazebo platform on the Ubuntu operating system. Computations are conducted on a device with an i7-14700f processor. The simulation environment is configured with a single RealSense camera and includes 55 objects selected from the Stanford 3D Scanning Repository (graphics.stanford.edu/data/3Dscanrep/), Linemod, and HomebrewedDB (bop.felk.cvut.cz/datasets/). The simulation environment is depicted in Fig. 8.

The Simulation experiment is based on two evaluation metrics: (1) Point Cloud Coverage: Sampling 10,000 points from the model file, traversing all model points, and calculating the proportion of model points that have a point in the input point cloud within a distance of 0.005m. (2) Computational Time: Measuring the time taken by the NBV planner to provide the next best view after receiving a frame input.

1) *Comparison experiments*: In Comparison experiments, our framework is compared with the voxel-based MCMF [2] (completeness-focused) NBV-net [6] and SCVP [7] (efficiency-focused), and the point cloud-based SEE [8].

In our experiments, both our framework and MCMF use an Octomap resolution of 0.03 meters. NBV-Net and SCVP, needing $32 \times 32 \times 32$ voxels, use a resolution of 0.006 meters. Our framework, MCMF, SEE, and NBV-Net have

800 candidate viewpoints, while SCVP has 32. Both SCVP and NBV-Net adopt the pre-trained models provided by the SCVP open-source project. Our global partition number β is 4, and T_{max} is 10. Since there is no issue with the robotic arm being unreachable in the simulation, we set the candidate viewpoint sampling space to a complete sphere. In this experiment, our framework processed an average of 2123.40 voxels and an average of 11.06 ellipsoids (including occupied and frontier).

TABLE I
COMPARISON EXPERIMENT RESULT

Framework	SEE	SCVP	NBVNET	MCMF	Ours
Coverage (%)	73.24	86.08	75.92	88.46	98.41
Time (s)	14.56	1.45	6.70	27.16	5.10

All frameworks receive data from the Realsense camera and adjust the camera's pose based on their NBV outputs for iteration, starting with the same initial pose. Each framework performs ten iterations, with point cloud coverage and computational time analyzed as key metrics.

Fig.9 shows that our framework outperforms other frameworks in the 55 objects, not only with the highest point cloud coverage but also with lower computational time. Tab. I presents the final average coverage and the computational time per iteration for the 55 objects. Compared to MCMF, the second-highest coverage framework, our coverage is 1.12 times higher, while the computation time is only 0.18 times that of MCMF, which is lower than the neural network-based framework NBV-Net.

2) *Ablation experiment*: The maximum number of ellipsoids T_{max} , the number of partitions β , and the initial viewpoints are all manually set. To validate the rationality of these settings, we designed three ablation experiments to evaluate different configurations.

We set β to 1 (disabling the global partition strategy) and varied T_{max} as 5, 10, 20, and 40, comparing them

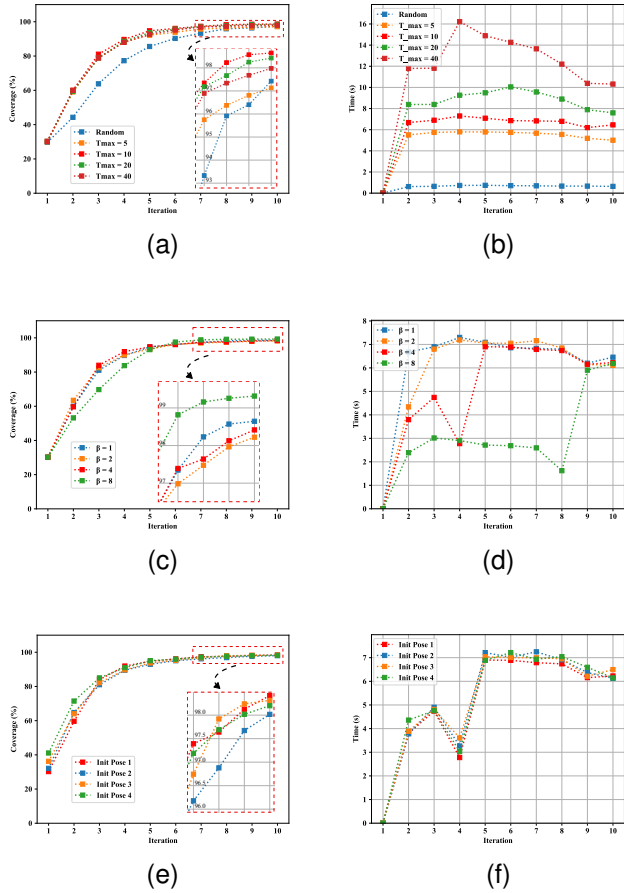


Fig. 10. Ablation experiment results for 55 objects in the simulation environment. (a)(c)(e) Average coverage per iteration. (b)(d)(f) Average compute time per iteration.

with the random selection strategy. The results shown in Fig.10(a)(b) indicate that the strategy is not sensitive to parameter selection, as different T_{max} values have minimal impact on convergence efficiency, and increasing T_{max} leads to a higher computational burden.

When T_{max} is set to 10, we performed a comparison for global partition numbers β of 1, 2, 4, and 8. The results show that a higher partition number improves the final convergence efficiency but at the cost of a slower convergence rate.

To verify the stability of our framework under different initial conditions, we tested it with $T_{max} = 10$ and $\beta = 4$ using four different initial viewpoints: $[0.9, 0, 0]$, $[0, 0.9, 0]$, $[0, 0, 0.9]$, and $[0, 0.63, 0.63]$. The results, as shown in Fig.10(e)(f), indicate that our framework is stable across different initial values.

B. Real-world experiments

As shown in Fig. 1, our experimental platform includes a self-made structured light 3D camera, a robotic arm with six degrees of freedom and a working range of 800 mm. and a 360-degree rotatable turntable to cover the entire hemispherical space of the object. The NBV planning framework and control programs run on a laptop with an i9-14700HX

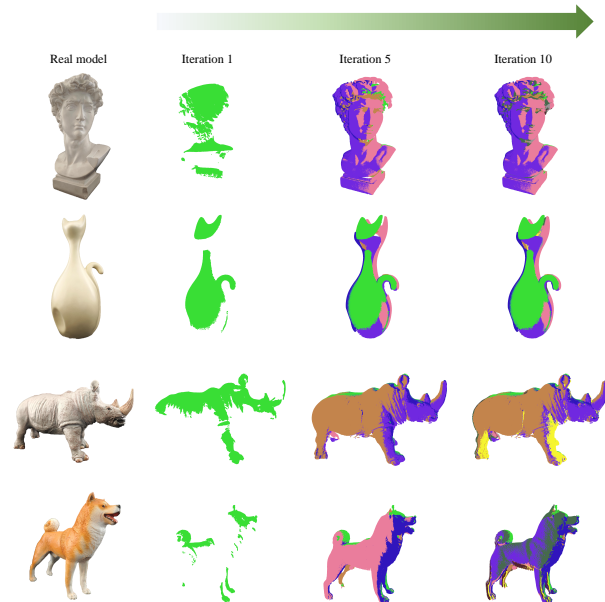


Fig. 11. The models used in the real-world experiment and their reconstruction results, from top to bottom: statue, vase, rhino and dog.

processor. The experiment used an Octomap resolution of 0.01m, with the number of partitions β set to 4, the maximum number of fitted ellipsoids T_{max} set to 50, the initial observation pose as shown in Fig. 1, and the number of iterations is 10. Reconstruction experiments on four objects of different sizes showed that our framework could achieve good results when reconstructing different objects, proving its feasibility.

TABLE II
OBJECT POINT CLOUD SIZE

Object name	statue	vase	rhino	dog
point cloud size	9655	3013	3857	2684

Since there is no ground truth for objects in real-world experiments, we adopted the SEE [8] by treating the final point cloud from the iterations as the ground truth to assess the convergence efficiency of the NBV process. The iteration process is shown in Fig. 12.

Tab. II presents the number of points in the registered point cloud after filtering with voxels of 0.005m edge length, which is used to indicate the size of the object. Fig. 12 and Tab. II show that objects like the vase and dog have lower computation times. Complex objects like the statue and rhino need more ellipsoids, increasing computation times. Although the point cloud size of the statue is more than twice that of the rhino, the computation time is similar, indicating that the computational cost of the framework is not significantly related to the object volume size.

V. CONCLUSION

This paper introduces a projection-based NBV planning framework that uses ellipsoids to represent objects in voxel

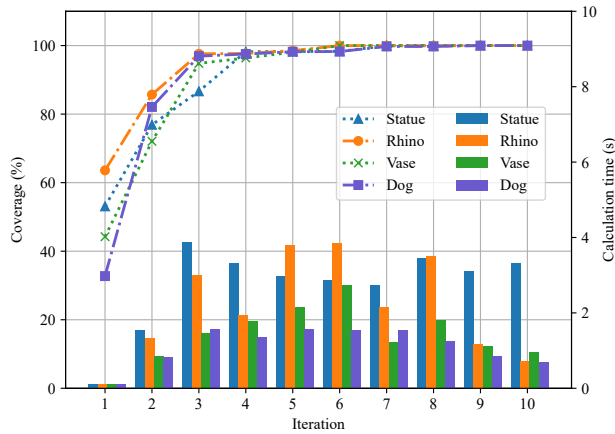


Fig. 12. Chart of result data from real-world experiments. The bar chart represents the computational time for each iteration, and the line chart represents the point cloud coverage after each iteration.

structures, replacing ray-casting with ellipsoid projection to select the optimal viewpoint. This approach not only provides higher coverage but also significantly reduces computational load, with both simulation and real-world experiments confirming its efficiency and feasibility. However, challenges remain in capturing complete surface data with structured light cameras on high-reflectivity materials or mutual reflections, which will guide future improvements to the NBV planning framework. In addition, efficiency-focused NBV planning frameworks should also focus on system movement efficiency, aiming for minimal movements and optimal global path planning.

REFERENCES

- [1] C. Connolly, "The determination of next best views," in *Proceedings. 1985 IEEE international conference on robotics and automation*, vol. 2. IEEE, 1985, pp. 432–435. 1, 2
- [2] S. Pan and H. Wei, "A global max-flow-based multi-resolution next-best-view method for reconstruction of 3d unknown objects," *IEEE Robotics and Automation Letters*, vol. 7, no. 2, pp. 714–721, 2021. 1, 2, 6
- [3] C. Potthast and G. S. Sukhatme, "A probabilistic framework for next best view estimation in a cluttered environment," *Journal of Visual Communication and Image Representation*, vol. 25, no. 1, pp. 148–164, 2014. 1, 2
- [4] A. Batinovic, T. Petrovic, A. Ivanovic, F. Petric, and S. Bogdan, "A multi-resolution frontier-based planner for autonomous 3d exploration," *IEEE Robotics and Automation Letters*, vol. 6, no. 3, pp. 4528–4535, 2021. 1, 2
- [5] A. Batinovic, A. Ivanovic, T. Petrovic, and S. Bogdan, "A shadowcasting-based next-best-view planner for autonomous 3d exploration," *IEEE Robotics and Automation Letters*, vol. 7, no. 2, pp. 2969–2976, 2022. 1, 2
- [6] M. Mendoza, J. I. Vasquez-Gomez, H. Taud, L. E. Sucar, and C. Reta, "Supervised learning of the next-best-view for 3d object reconstruction," *Pattern Recognition Letters*, vol. 133, pp. 224–231, 2020. 1, 2, 6
- [7] S. Pan, H. Hu, and H. Wei, "Scvp: Learning one-shot view planning via set covering for unknown object reconstruction," *IEEE Robotics and Automation Letters*, vol. 7, no. 2, pp. 1463–1470, 2022. 1, 2, 6
- [8] R. Border and J. D. Gammell, "The surface edge explorer (see): A measurement-direct approach to next best view planning," *The International Journal of Robotics Research*, p. 02783649241230098, 2024. 1, 2, 6, 7
- [9] R. Zeng, W. Zhao, and Y.-J. Liu, "Pc-nbv: A point cloud based deep network for efficient next best view planning," in *2020 IEEE/RSJ International Conference on Intelligent Robots and Systems (IROS)*. IEEE, 2020, pp. 7050–7057. 2
- [10] H. Dhami, V. D. Sharma, and P. Tokekar, "Pred-nbv: Prediction-guided next-best-view planning for 3d object reconstruction," in *2023 IEEE/RSJ International Conference on Intelligent Robots and Systems (IROS)*. IEEE, 2023, pp. 7149–7154. 2
- [11] J. I. Vasquez-Gomez, L. E. Sucar, and R. Murrieta-Cid, "View planning for 3d object reconstruction with a mobile manipulator robot," in *2014 IEEE/RSJ International Conference on Intelligent Robots and Systems*. IEEE, 2014, pp. 4227–4233. 2
- [12] S. Song, D. Kim, and S. Jo, "Online coverage and inspection planning for 3d modeling," *Autonomous Robots*, vol. 44, no. 8, pp. 1431–1450, 2020. 2
- [13] B. Zhou, Y. Zhang, X. Chen, and S. Shen, "Fuel: Fast uav exploration using incremental frontier structure and hierarchical planning," *IEEE Robotics and Automation Letters*, vol. 6, no. 2, pp. 779–786, 2021. 2
- [14] J. I. Vasquez-Gomez, L. E. Sucar, R. Murrieta-Cid, and J.-C. Herrera-Lozada, "Tree-based search of the next best view/state for three-dimensional object reconstruction," *International Journal of Advanced Robotic Systems*, vol. 15, no. 1, p. 1729881418754575, 2018. 2
- [15] D. Deng, Z. Xu, W. Zhao, and K. Shimada, "Frontier-based automatic-differentiable information gain measure for robotic exploration of unknown 3d environments," *arXiv preprint arXiv:2011.05288*, 2020. 2
- [16] M. Roberts, D. Dey, A. Truong, S. Sinha, S. Shah, A. Kapoor, P. Hanrahan, and N. Joshi, "Submodular trajectory optimization for aerial 3d scanning," in *Proceedings of the IEEE International Conference on Computer Vision*, 2017, pp. 5324–5333. 2
- [17] C. Peng and V. Isler, "Adaptive view planning for aerial 3d reconstruction," in *2019 International Conference on Robotics and Automation (ICRA)*. IEEE, 2019, pp. 2981–2987. 2
- [18] S. Wu, W. Sun, P. Long, H. Huang, D. Cohen-Or, M. Gong, O. Deussen, and B. Chen, "Quality-driven poisson-guided autoscanning," *empty*, 2014. 2
- [19] Y. Ran, J. Zeng, S. He, J. Chen, L. Li, Y. Chen, G. Lee, and Q. Ye, "Neurar: Neural uncertainty for autonomous 3d reconstruction with implicit neural representations," *IEEE Robotics and Automation Letters*, vol. 8, no. 2, pp. 1125–1132, 2023. 2
- [20] S. Lee, L. Chen, J. Wang, A. Liniger, S. Kumar, and F. Yu, "Uncertainty guided policy for active robotic 3d reconstruction using neural radiance fields," *IEEE Robotics and Automation Letters*, vol. 7, no. 4, pp. 12070–12077, 2022. 2, 5
- [21] L. Jin, X. Chen, J. Rückin, and M. Popović, "Neu-nbv: Next best view planning using uncertainty estimation in image-based neural rendering," in *2023 IEEE/RSJ International Conference on Intelligent Robots and Systems (IROS)*. IEEE, 2023, pp. 11305–11312. 2
- [22] R. Monica and J. Aleotti, "Surfel-based next best view planning," *IEEE Robotics and Automation Letters*, vol. 3, no. 4, pp. 3324–3331, 2018. 2
- [23] B. Kerbl, G. Kopanas, T. Leimkühler, and G. Drettakis, "3d gaussian splatting for real-time radiance field rendering," *ACM Trans. Graph.*, vol. 42, no. 4, pp. 139–1, 2023. 2, 4
- [24] J. Amanatides, A. Woo *et al.*, "A fast voxel traversal algorithm for ray tracing," in *Eurographics*, vol. 87, no. 3. Citeseer, 1987, pp. 3–10. 3
- [25] K. Fauerby, "Improved collision detection and response," *Peroxide Entertainment*, 2003. 4
- [26] G. Schwarz, "Estimating the dimension of a model," *The annals of statistics*, pp. 461–464, 1978. 4
- [27] B. Gärtner and S. Schönherr, "Smallest enclosing ellipses: fast and exact," *empty*, 1997. 4
- [28] R. Hartley and A. Zisserman, *Multiple view geometry in computer vision*. Cambridge university press, 2003. 5
- [29] P. J. Besl and N. D. McKay, "Method for registration of 3-d shapes," in *Sensor fusion IV: control paradigms and data structures*, vol. 1611. Spie, 1992, pp. 586–606. 5